biosensors

MDPI

Article

Polydopamine-Coated Co_3O_4 Nanoparticles as an Efficient Catalase Mimic for Fluorescent Detection of Sulfide Ion

Trung Hieu Vu, Phuong Thy Nguyen and Moon Il Kim *

Department of BioNano Technology, Gachon University, 1342 Seongnamdae-ro, Sujeong-gu, Seongnam 13120, Republic of Korea

* Correspondence: moonil@gachon.ac.kr; Tel.: +82-31-750-8563

Abstract: Surface engineering of nanozymes has been recognized as a potent strategy to improve their catalytic activity and specificity. We synthesized polydopamine-coated Co_3O_4 nanoparticles (PDA@Co_3O_4 NPs) through simple dopamine-induced self-assembly and demonstrated that these NPs exhibit catalase-like activity by decomposing H_2O_2 into oxygen and water. The activity of PDA@Co_3O_4 NPs was approximately fourfold higher than that of Co_3O_4 NPs without PDA, possibly due to the additional radical scavenging activity of the PDA shell. In addition, PDA@Co_3O_4 NPs were more stable than natural catalase under a wide range of pH, temperature, and storage time conditions. Upon the addition of a sample containing sulfide ion, the activity of PDA@Co_3O_4 NPs was significantly inhibited, possibly because of increased mass transfer limitations via the absorption of the sulfide ion on the PDA@Co_3O_4 NP surface, along with NP aggregation which reduced their surface area. The reduced catalase-like activity was used to determine the levels of sulfide ion by measuring the increased fluorescence of the oxidized terephthalic acid, generated from the added H_2O_2. Using this strategy, the target sulfide ion was sensitively determined to a lower limit of 4.3 μM and dynamic linear range of up to 200 μM. The fluorescence-based sulfide ion assay based on PDA@Co_3O_4 NPs was highly precise when applied to real tap water samples, validating its potential for conveniently monitoring toxic elements in the environment.

Keywords: polydopamine coating; cobalt oxide nanoparticles; catalase-like nanozyme; sulfide ion detection; fluorescent biosensors

Citation: Vu, T.H.; Nguyen, P.T.; Kim, M.I. Polydopamine-Coated Co_3O_4 Nanoparticles as an Efficient Catalase Mimic for Fluorescent Detection of Sulfide Ion. *Biosensors* **2022**, *12*, 1047. https://doi.org/10.3390/bios12111047

Received: 20 October 2022
Accepted: 16 November 2022
Published: 19 November 2022

1. Introduction

Sulfide ions (S^{2-}), which are among the most harmful contaminants, are extensively released into aqueous environments through various agricultural and industrial processes. These ions can exist in the human body and take part in the antioxidant process in liver and lung, or act as vasodilators [1–3]. Importantly, an imbalance in S^{2-} levels has been implicated in various diseases such as Alzheimer's disease, Down's syndrome, hyperglycemia, and liver cirrhosis [4–7]. Abnormally high levels of S^{2-} can directly threaten both the ecological environment and human health. To date, many methods for detecting S^{2-} have been developed, such as gas chromatography [8,9], titration [10], extraction [11], colorimetric [12,13], electrochemical [14], and fluorometric assays [15]. However, these methods are often time-consuming because of the sample pre/post treatments required, involved complicated assay procedures, and need for qualified operators [16]. Thus, more rapid, convenient, selective, sensitive, and reliable analytical methods for S^{2-} detection are urgently needed.

Catalase, which is commonly found in most aerobic organisms, plays a crucial role in protecting cells against oxidative damage, by decomposing H_2O_2 into non-harmful O_2 and H_2O [17]. Similar to other natural enzymes, catalase is unstable under harsh conditions, is costly to produce and purify, and is difficult to recycle. To overcome these limitations, studies aimed at developing an appropriate catalase mimic from nanomaterials exhibiting

enzyme-like activities (nanozymes) have gained attention. To date, several types of catalase-mimicking nanozymes have been reported, such as cerium oxide nanoparticles [18], iron oxide NPs [19], and cobalt oxide (Co_3O_4) NPs [20,21]. Among these, Co_3O_4 NPs showed morphology-dependent catalase-like activity; however, few studies have reported their surface engineering, which is an efficient approach for engineering nanozymes with improved activity [22,23].

Herein, we developed polydopamine (PDA)-coated Co_3O_4 NPs (PDA@Co_3O_4 NPs) as highly active catalase-mimicking nanozymes and applied these NPs in fluorescent detection of S^{2-}. PDA can be produced through self-polymerization of dopamine (DA) without the involvement of any organic solvent, yielding unique adhesion properties based on its active catechol and alkane groups, to facilitate substrate adsorption and product desorption in diverse reactions [24–26]. The synthesized PDA@Co_3O_4 NPs showed high catalase-like activity in degrading H_2O_2, which inhibited the formation of extremely fluorescent 2-hydroxy terephthalic acid, to decrease the fluorescent signal. Interestingly, S^{2-} in the sample may interact with PDA@Co_3O_4 NPs, resulting in decreased catalase-like activity via increased substrate transfer limitations and a decreased available surface area for catalytic events. We detected the target S^{2-} in a PDA@Co_3O_4 NPs-based fluorescent assay and investigated various analytical characteristics, such as selectivity, sensitivity, stability, and practical utility along with the detection precision.

2. Materials and Methods

2.1. Reagents and Materials

Cobalt (II) sulfate heptahydrate ($CoSO_4 \cdot 7H_2O$), DA hydrochloride, trizma hydrochloride (Tris-HCl), terephthalic acid (TA), sodium acetate (NaAc), sodium borohydride ($NaBH_4$), and sodium sulfide (Na_2S) were purchased from Sigma-Aldrich (St. Louis, MO, U.S.A.). Hydrogen peroxide was obtained from Samchun Chemical (Seoul, Korea). All solutions were prepared in deionized water purified using a Milli-Q Purification System (Millipore, Billerica, MA, U.S.A.).

2.2. Synthesis and Characterization of PDA@Co_3O_4 NPs

PDA@Co_3O_4 NPs were synthesized following a previously reported method for DA-induced self-assembly with some modifications [25]. First, 250 mg $CoSO_4 \cdot 7H_2O$ was dissolved in 50 mL of Tris-HCl buffer (pH 8.5) at 25 °C. DA (1 mg/mL) was added to the solution, followed by sonication at a frequency of 40 kHz and power of 160 W for 20 min. Next, 2 mL of 50 mM $NaBH_4$ was added, and the mixture was incubated at 60 °C for 4 h. The pellet was collected by a centrifugation (8000× *g*, 8 min), followed by freeze-drying to obtain the resulting black powders. Bare Co_3O_4 NPs without a PDA shell were synthesized using the same procedures except that H_2O was added instead of DA.

The synthesized materials were analyzed using scanning electron microscopy (SEM) and transmission electron microscopy (TEM), using a field emission scanning electron microscope (Hitachi S-4700, Tokyo, Japan) and transmission electron microscope (FEI Tecnai, OR), respectively. Elemental composition was analyzed using an energy-dispersive spectrometer (EDX) (Bruker, Billerica, MA, U.S.A.). For SEM analyses, the suspension of sonicated NPs was dried on a silicon wafer. For TEM analyses, 5 µL of the suspension of sonicated NPs was dropped onto a carbon-coated copper TEM grid (Electron Microscopy Sciences, Hatfield, U.K.) followed by drying overnight at room temperature (RT). Fourier transform infrared (FT-IR) spectra of the NPs were obtained using an FT-IR spectrophotometer (FT/IR-4600, JASCO, Tokyo, Japan). X-ray diffraction (XRD) and X-ray photoelectron spectroscopy (XPS) were conducted using an X-ray diffractometer (D/MAX-2500, Rigaku Corporation, Tokyo, Japan) and XPS reader (Gemini, Molecular Devices, Sunnyvale, CA, U.S.A.), respectively. The size distribution of the NPs was determined using dynamic light scattering (DLS) (Zetasizer, Malvern Instruments, Malvern, U.K.).

2.3. Evaluation of Enzyme-Like Activity of PDA@Co_3O_4 NPs

Catalase-like activity of PDA@Co_3O_4 NPs was examined by using TA as a fluorescent probe in the presence of H_2O_2. In a standard assay, PDA@Co_3O_4 NPs or bare Co_3O_4 NPs (both at 100 μg/mL), H_2O_2 (20 mM), and TA (0.625 mM) were incubated in NaAc buffer solution (0.1 M, pH 6.0) for 20 min at RT under UV irradiation at 254 nm using a UV transilluminator (Core-Bio System, Seoul, Korea). The fluorescent signal was monitored using a microplate reader (Synergy H1, BioTek, Winooski, VT, U.S.A.) at excitation and emission wavelengths of 315 and 420 nm, respectively. The effects of the PDA@Co_3O_4 NP concentration on their catalytic activity were examined following the same procedures but with varying concentrations of PDA@Co_3O_4 NPs (0, 6.25, 12.5, 25, 50, 100, 150, 200, 250, and 300 μg/mL). The effects of the reaction pH and temperature on the catalytic activity of PDA@Co_3O_4 NPs and natural free catalase were evaluated over wide pH (3.0–9.0) and temperature (4–80 °C) ranges. Stabilities of PDA@Co_3O_4 NPs and free catalase were investigated by incubating them for 8 h in NaAc buffer at various pH values (3.0–10.0) at RT or temperatures (4–80 °C) at pH 6.0. The long-term stabilities of PDA@Co_3O_4 NPs and free catalase were also evaluated by incubating them in NaAc buffer (pH 6.0) under static conditions at RT. The initial activities were determined by measuring the fluorescence intensity under standard assay conditions, and relative activity (%) was determined by calculating the ratio of residual to initial activity. Fluorescent images were acquired using a fluorescence imaging system (Kodak, Tokyo, Japan).

Steady-state kinetic parameters of the catalase-like activity of PDA@Co_3O_4 NPs were determined based on oxygen production measured using a dissolved oxygen meter (Eutech DO 6+, Thermo Fisher Scientific, Waltham, MA, U.S.A.). Various concentrations of H_2O_2 solution were added to NaAc buffer and continually stirred until the dissolved oxygen value was stable, followed by addition of PDA@Co_3O_4 NPs (100 μg/mL). Dissolved oxygen concentrations were recorded over time, and the initial reaction rates were calculated according to the Michaelis–Menten equation, $v = V_{max} \times [S]/(K_m + [S])$, where v is the initial velocity, V_{max} is the maximum reaction velocity, [S] is the concentration of substrate H_2O_2, and K_m is the Michaelis constant.

Peroxidase (POD)-like activities of PDA@Co_3O_4 NPs and bare Co_3O_4 NPs were assessed by measuring the oxidation of 3,3′,5,5′-tetramethylbenzidine (TMB) in the presence of H_2O_2. Typically, PDA@Co_3O_4 NPs or bare Co_3O_4 NPs (both at 100 μg/mL) were added to NaAc buffer (0.1 M, pH 4.0) containing TMB (0.5 mM), followed by incubation for 5 min at RT. The blue color intensity was recorded at 652 nm using a microplate reader (Synergy H1). Oxidase (OXD)-like activities were measured following the same procedure as in the POD-assay but in the absence of H_2O_2. Superoxide dismutase (SOD)-like activities were evaluated by measuring the reduction in cytochrome C at 550 nm in the presence of superoxide radicals ($O_2^{\bullet -}$). Xanthine and xanthine oxidase (XO) were used as the source to generate $O_2^{\bullet -}$. Briefly, PDA@Co_3O_4 NPs (100 μg/mL) was added to phosphate buffer (0.05 m, pH 7.4) containing xanthine (0.05 mM), XO (0.15 mU/mL), and cytochrome C (0.01 mM), followed by incubation for 10 min at RT in the dark. The resultant solutions were centrifuged, and used to monitor the absorbance intensities at 550 nm using a microplate reader (Synergy H1).

2.4. Detection of S^{2-} Using PDA@Co_3O_4 NPs

Detection of S^{2-} using the catalase-like activity of PDA@Co_3O_4 NPs was performed as follows. First, aqueous solutions containing various concentrations of sodium sulfide were prepared as the S^{2-} source (0–600 μM). The S^{2-} sample solutions were added to an assay mixture containing PDA@Co_3O_4 NPs (100 μg/mL), H_2O_2 (20 mM), and TA (0.625 mM) in NaAc buffer solution (0.1 M, pH 6.0). The reaction mixture was incubated for 20 min at RT under UV irradiation (254 nm), and the resulting fluorescent signals were recorded as aforementioned. The limit of detection (LOD) values were calculated as 3 times of standard deviation (SD) of blank value over the slope of the calibration curve.

To demonstrate the practical utility of the proposed assay, real tap water samples were spiked with S^{2-}. For this assay, tap water samples were first collected from the laboratory and filtered through a syringe membrane with a pore size of 0.45 μm to eliminate undesirable molecules. Then, predetermined amounts of S^{2-} were added to the collected tap water samples to prepare spiked samples containing final S^{2-} concentrations of 50, 100, and 200 μM. Finally, the concentrations of S^{2-} in the spiked tap water samples were determined as described above. To measure the accuracy and reproducibility of the assay, we calculated the recovery rate (recovery rate (%) = measured value/actual value × 100) and the coefficient of variation (CV (%) = SD/average × 100), from the six independent assay results.

3. Results and Discussion

3.1. Synthesis of PDA@Co_3O_4 NPs as an Efficient Catalase Mimic to Detect S^{2-}

The procedure used for DA-u of DA to form a PDS shell on the Co_3O_4 NPs, would have enhanced catalase-like activity with help of additional radical scavenging activity of the PDA shell. Based on this enhanced activity, a highly sensitive system for S^{2-} detection was developed. The high catalase-like activity of PDA@Co_3O_4 NPs induced inhibition of the formation of fluorescent 2-hydroxyl TA in the presence of H_2O_2, yielding a very low fluorescence background. Importantly, S^{2-} in the sample solution selectively interacted with the surface of PDA@Co_3O_4 NPs, resulting in a significant reduction in their catalase-like activity and concomitant increase in fluorescence via the facilitated formation of 2-hydroxyl TA. Specifically, S^{2-} was predicted to be adsorbed on the surface of PDA@Co_3O_4 NPs, causing them to aggregate and leading to mass transfer limitations. These factors significantly reduced the catalase-like activity of PDA@Co_3O_4 NPs and increased the fluorescence signal proportionally to the amount of target S^{2-} (Figure 1).

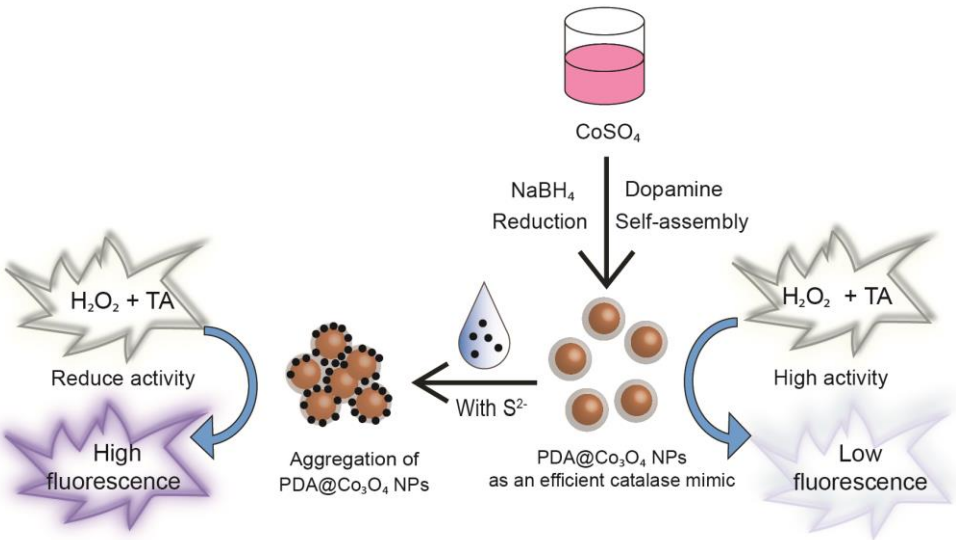

Figure 1. Schematic illustration of the synthesis of catalase-like PDA@Co_3O_4 NPs and their application to fluorescently detect sulfide ion (S^{2-}).

3.2. Characterization of PDA@Co_3O_4 NPs

Structural characteristics of PDA@Co_3O_4 NPs were analyzed and compared with those of bare Co_3O_4 NPs without a PDA shell by TEM and SEM images. Bare Co_3O_4 NPs had spherical shape with 20.03 ± 2.82 nm diameter, calculated from their TEM images, and importantly, relatively thick (~15 nm) shells were clearly observed outside the core NPs from the PDA@Co_3O_4 NPs (Figure 2a,b). In basic conditions, DA is known to easily interact with the surface of the NPs by a variety of interactions, including electrostatic interaction, metal coordination, and hydrogen bonding, and induce its polymerization

among another DA monomers [25–30]. Thus, it was believed that the layer around the Co_3O_4 NPs was PDA shell, as also clearly observed in the SEM images (Figure S1 in Supplementary Materials). As the concentrations of DA increased, the thickness of polymeric shell concomitantly increased, which was similar to the previous studies (Figure S2) [25,31]. High-resolution TEM (HRTEM) imaging and selected area electron diffraction imaging (SAED) demonstrated the presence of crystalline Co_3O_4 in PDA@Co_3O_4 NPs, which fit well with the reported data (JCPDS no. 76–1802) (Figure 2c,d). EDX images also proved the presence of Co, N, and O, which were well distributed throughout the material (Figure 2e). The elemental composition ratios within the PDA@Co_3O_4 NPs are provided in Table S1.

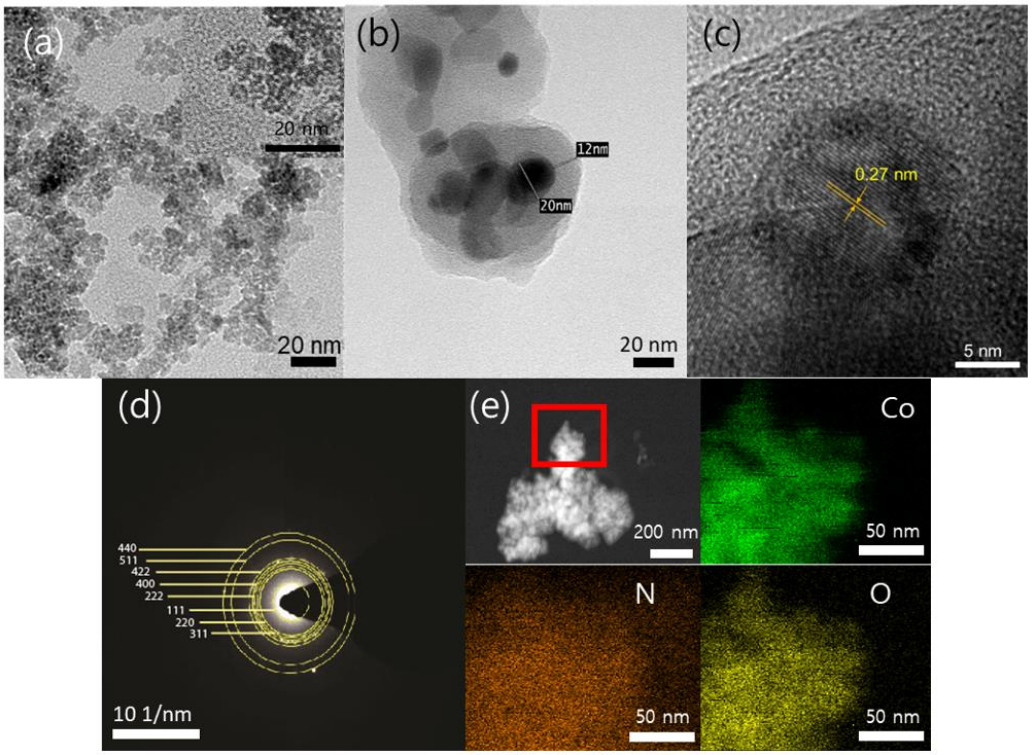

Figure 2. TEM images of (**a**) bare Co_3O_4 NPs and (**b**) PDA@Co_3O_4 NPs. PDA@Co_3O_4 NPs were additionally analyzed by (**c**) HRTEM, (**d**) SAED, and (**e**) EDX mapping images of the selected region (shown as red rectangle).

XRD, FT-IR, and XPS analyses were additionally performed to characterize the synthesized PDA@Co_3O_4 NPs in detail. The XRD patterns clearly confirmed the presence of crystalline Co_3O_4, and the peaks of PDA@Co_3O_4 NPs kept nearly the same intensity compared with those of bare Co_3O_4 NPs, proving that the PDA layer does not negatively affect the crystalline structure of core Co_3O_4 NPs (Figure 3a). The FT-IR spectra confirmed the chemical structure of PDA@Co_3O_4 NPs, with the peaks corresponding to C-O stretch (1295 cm^{-1}), N-H stretch (1510 cm^{-1}), C-H stretch (around 3000 cm^{-1}), and aromatic ring (1605 cm^{-1}), which demonstrated the presence of the PDA layer on the surface of Co_3O_4 NPs (Figure 3b). The PDA peaks around 3400 cm^{-1}, which corresponded to the hydrogen bonds of O-H and N-H, were shifted in PDA@Co_3O_4 NPs, proving the interaction between Co_3O_4 NPs and catechol hydroxyl group of PDA [24]. Moreover, XPS analysis revealed peaks corresponding to C, N, O, and Co at 283.37, 398.23, 530.34, and 779.3 eV, respectively (Figure S3). The appearance of C, N, and O elements was attributed to the presence of PDA on the Co_3O_4 NP surface. In addition, the electronic configurations of the O and Co peaks supported the presence of Co_3O_4 NPs (Figure 3c,d) [31]. All these characterizations confirm that PDA@Co_3O_4 NPs were successfully formed by incorporation of a PDA layer on crystalline Co_3O_4 NPs.

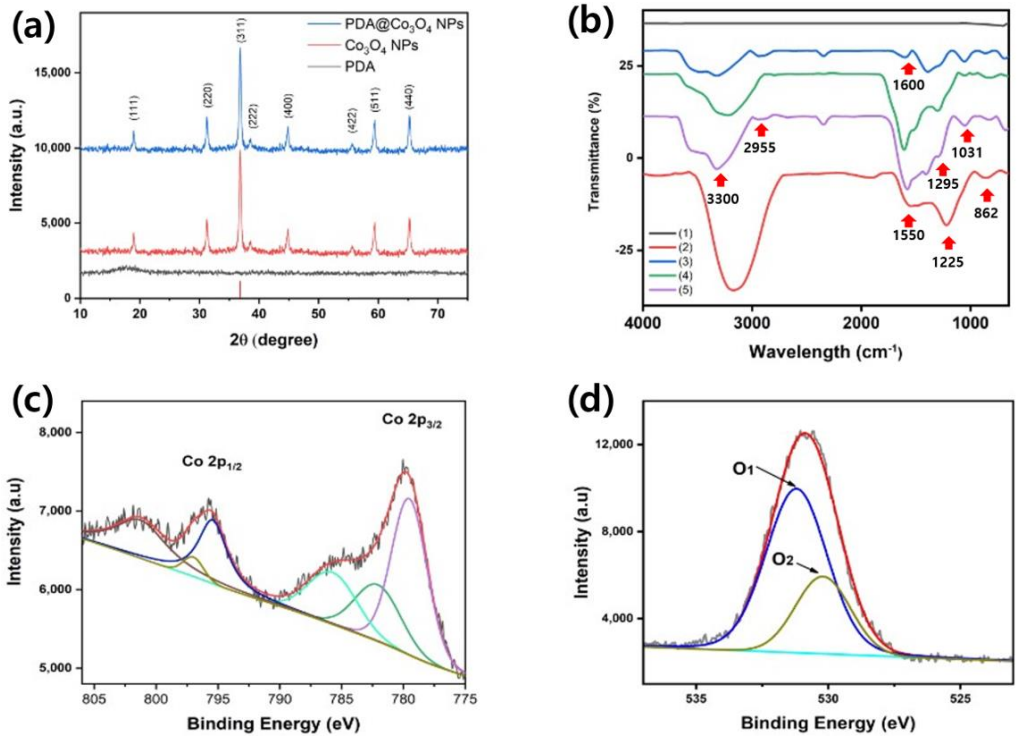

Figure 3. (**a**) XRD spectra, (**b**) FT-IR spectra of bare Co_3O_4 NPs, PDA, 0.5−PDA@Co_3O_4 NPs, 1−PDA@Co_3O_4 NPs, and 2−PDA@Co_3O_4 NPs (denoted as 1, 2, 3, 4, and 5, respectively), and high-resolution XPS spectra of PDA@Co_3O_4 NPs for (**c**) Co 2p and (**d**) O 1s.

3.3. Evaluation of the Catalase-like Activity of PDA@Co_3O_4 NPs

Catalase-like activities of PDA@Co_3O_4 NPs and control Co_3O_4 NPs were evaluated via the decomposition of H_2O_2 by monitoring the changes in the fluorescent intensities of TA. In the absence of catalase mimics, H_2O_2 under UV irradiation produced hydroxyl radicals which further reacted with TA, generating highly fluorescent 2-hydroxy TA. PDA@Co_3O_4 NPs or bare Co_3O_4 NPs catalyzed the decomposition of H_2O_2 to H_2O and O_2, resulting in a decrease in the fluorescent signal, and importantly, PDA@Co_3O_4 NPs exhibited much higher activity, which was up to approximately fourfold higher than that of bare Co_3O_4 NPs (Figure 4a,b). The thickness of the PDA layer significantly affected the catalase-like activity of the materials (Figure 4b). PDA@Co_3O_4 NPs with 2 mg/mL DA (2-PDA@Co_3O_4 NPs) and PDA@Co_3O_4 NPs with 1 mg/mL DA (1-PDA@Co_3O_4 NPs) exhibited higher activity than that of PDA@Co_3O_4 NPs with 0.5 mg/mL DA (0.5-PDA@Co_3O_4 NPs), and the activity difference between 2-PDA@Co_3O_4 NPs and 1-PDA@Co_3O_4 NPs was not significant. Thus, 1-PDA@Co_3O_4 NPs were chosen and used for further studies. We also investigated the other oxidoreductases (POD, OXD, and SOD)-like activities of PDA@Co_3O_4 NPs and bare Co_3O_4 NPs (Figure S4). Both PDA@Co_3O_4 NPs and bare Co_3O_4 NPs were unable to remove the $O_2^{\bullet-}$ produced by the xanthine and XO reaction. In terms of POD- and OXD-like activity, the PDA@Co_3O_4 NPs, unlike Co_3O_4 NPs, could not oxidize TMB to produce blue-color product (oxidized TMB), which can be measured at 652 mm. It indicated that the developed PDA@Co_3O_4 NPs almost solely exhibited high catalase-like activity, which is beneficial for their utilization in catalase-mediated applications.

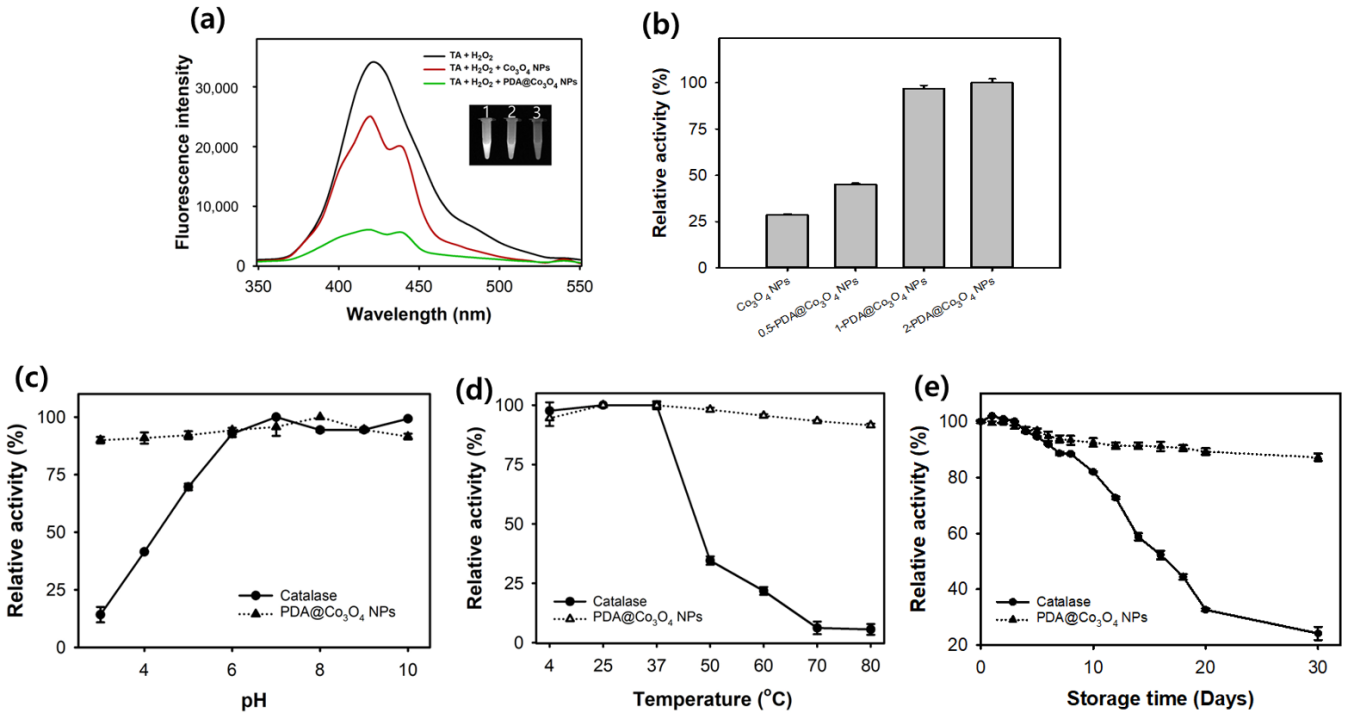

Figure 4. Evaluation of the catalase-like activity of PDA@Co_3O_4 NPs. (**a**) Catalase-like activity of bare Co_3O_4 NPs (red line) and PDA@Co_3O_4 NPs (green line). Insert fluorescent image indicates (1) control, (2) bare Co_3O_4 NPs, and (3) PDA@Co_3O_4 NPs. (**b**) Comparison of the catalase-like activity among 0.5-PDA@Co_3O_4 NPs, 1- PDA@Co_3O_4 NPs, and 2-PDA@Co_3O_4 NPs. Comparisons of the stability between PDA@Co_3O_4 NPs and natural catalase regarding (**c**) pH, (**d**) temperature, and (**e**) storage time at RT.

Several parameters affecting the activity, such as the concentrations of PDA@Co_3O_4 NPs, reaction pH, and temperature were examined to obtain the optimal reaction conditions (Figure S5). With increasing concentrations of PDA@Co_3O_4 NPs, the fluorescence intensity gradually decreased, and 100 μg/mL of PDA@Co_3O_4 NPs was selected for further experiments (Figure S5a). Similar to natural catalase, the activity of PDA@Co_3O_4 NPs was dependent on the reaction pH and temperature, and pH 6 and RT were found to be the optimal assay conditions (Figure S5b,c). PDA@Co_3O_4 NPs showed high activity (over 60%) over broad pH and temperature ranges, whereas natural catalase did not show considerable activity (below 40%) under harsh conditions (acidic or basic pH, and high temperature over 60 °C). This difference may have resulted from the coated PDA layer, which shows additional catalase-like activity even under harsh reaction environments [32].

Under the optimized conditions, stabilities of PDA@Co_3O_4 NPs, depending on the pH, temperature, and storage time at RT, were assessed and compared with those of natural catalase. As expected, under all conditions, PDA@Co_3O_4 NPs clearly showed improved stabilities, maintaining over 90% of their initial activity, while natural catalase lost over half of its activity under harsh conditions (acidic pH below 4, temperature over 50 °C, and storage over 15 days) (Figure 4c–e). The clear improvement in the stability of PDA@Co_3O_4 NPs is beneficial for their practical applications.

Steady-state kinetic assays of PDA@Co_3O_4 NPs were performed to determine the Michaelis constant (K_m) and maximal reaction velocity (V_{max}), which are important to elucidate reaction mechanism [33]. According to the Michaelis–Menten curve obtained using different H_2O_2 concentrations and the corresponding Lineweaver–Burk plot, the kinetic parameters were calculated and compared with those of previously reported values from other Co_3O_4-based catalase mimics and natural catalase (Figure S6 and Table S2). The K_m value of PDA@Co_3O_4 NPs was 22.1 mM, which was over twofold lower than that of

natural catalase and among the lowest values reported for Co_3O_4-based catalase mimics. These outcomes suggest that PDA@Co_3O_4 NPs have higher affinity toward the substrate H_2O_2 compared with that of catalase and most Co_3O_4-based nanozymes, possibly because of the PDA shell. The V_{max} of PDA@Co_3O_4 NPs was lower than that of natural catalase but higher than those of recently reported Co_3O_4 nanozymes. These observations indicate that combining PDA and Co_3O_4 NPs enhanced the catalase-mimicking performance of Co_3O_4 NPs.

3.4. Analytical Capabilities of PDA@Co_3O_4 NPs for the Detection of Sulfide Ion

PDA@Co_3O_4 NPs with enhanced catalase-like performances were utilized to fluorescently detect environmentally harmful S^{2-}. In the absence of S^{2-}, TA-mediated fluorescence was significantly decreased because of the high catalase-like activity of PDA@Co_3O_4 NPs (Figure 5a). In the presence of S^{2-}, the fluorescence was clearly restored due to the significant reduction in the activity of PDA@Co_3O_4 NPs. The S^{2-}-mediated reduction in activity may have occurred because of the interaction of S^{2-} on the PDA surface and subsequent inhibition of H_2O_2 decomposition, resulting in an increased TA-mediated fluorescence signal. The PDA@Co_3O_4 NPs-based S^{2-} biosensing system showed high selectivity for S^{2-} (50 μM), while diverse interfering compounds such as small molecules (glucose, urea), biothiols (glutathione, cysteine), and common ions (Mg^{2+}, NH_4^+, Ca^{2+}, Cl^-) did not have any considerable signal (below the threshold line), even at tenfold higher concentrations (Figure 5b), confirming that the biosensing strategy selectively detected target S^{2-}. On increasing the concentrations of S^{2-}, fluorescence intensity gradually increased (Figure S7). From the analysis of dose–response curves, the LOD was calculated as low as 4.3 μM with the linear range up to 200 μM (Figure 5c,d), which is sufficient for practical S^{2-} biosensing in the field [34,35].

We speculated that the possible mechanism of the PDA@Co_3O_4 NP-mediated S^{2-} biosensing system was that the target S^{2-} aggressively adsorbed on PDA@Co_3O_4 NPs and caused substrate transfer limitations via their aggregation, yielding reduced catalase-like activity. To confirm this prediction, the size of the PDA@Co_3O_4 NPs was determined in the presence and absence of S^{2-} (Figure S8). The experiments clearly showed that the PDA@Co_3O_4 NPs were aggregated in the presence of S^{2-}, leading to larger particle sizes (around 800–1000 nm), whereas non-aggregated PDA@Co_3O_4 NPs were less than 500 nm in size. This aggregation may reduce the surface area of PDA@Co_3O_4 NPs and, thus, reduce the response towards H_2O_2 [36].

Finally, to investigate the practical biosensing capability of the developed system, the PDA@Co_3O_4 NP-based assay was used to determine S^{2-} in spiked tap water samples, prepared at three concentrations of S^{2-} (50, 100, 200 μM). The biosensor quantified S^{2-} in tap water with good precision and accuracy, with CVs from 3.56 to 6.67% and recovery from 99.75 to 102.43% (Table 1), validating the excellent reproducibility and reliability. These results suggest that the PDA@Co_3O_4 NP-based fluorometric biosensor can be used as an analytical system for the determination of S^{2-} in real aqueous environments.

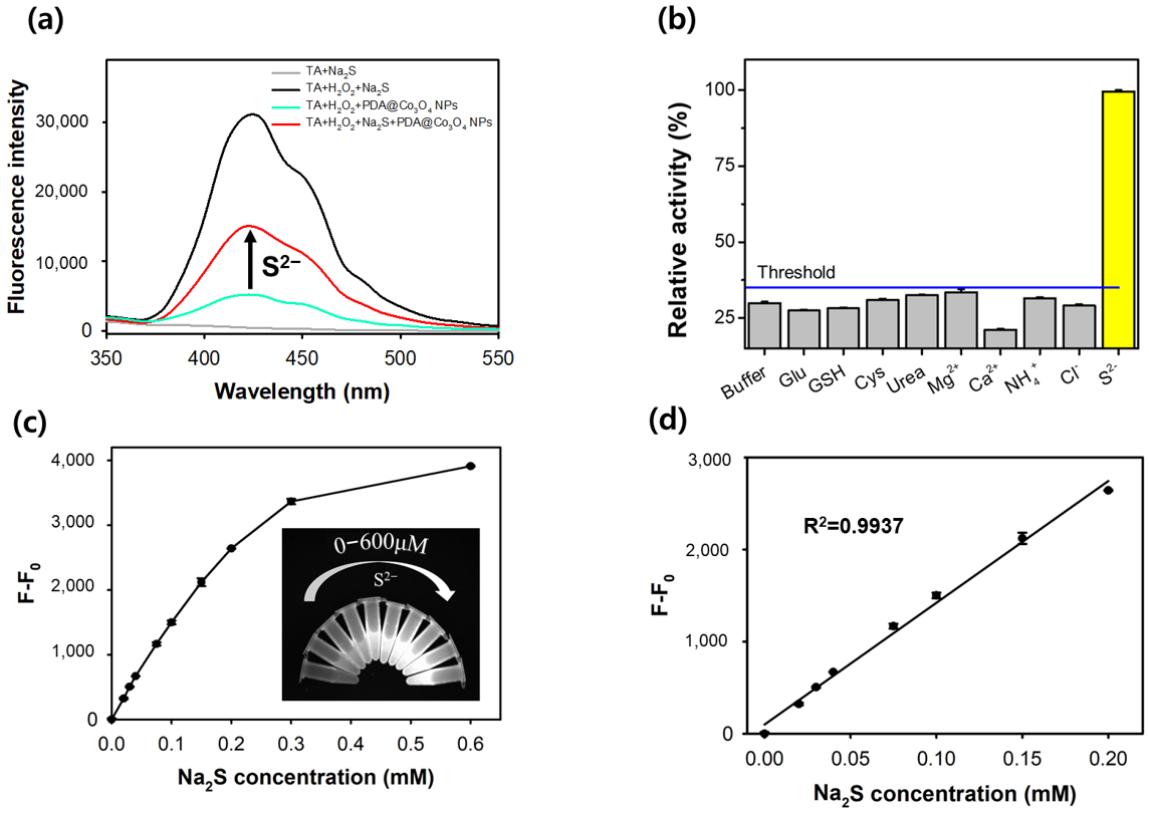

Figure 5. Analytical capabilities of PDA@Co_3O_4 NPs for the detection of S^{2-}. (**a**) Fluorescence spectra for the inhibition of catalase-like activity of PDA@Co_3O_4 NPs by S^{2-}. (**b**) Selectivity of PDA@Co_3O_4 NPs-based biosensor toward S^{2-}. (**c**) Dose–response curve with real florescent images and (**d**) its corresponding linear calibration plot for the determination of diverse concentrations of S^{2-} using the PDA@Co_3O_4 NPs–based biosensor.

Table 1. Detection precision of PDA@Co_3O_4 NPs-based biosensor for the quantitative determination of S^{2-} spiked in real tap water samples.

Compound	Spiked Level (μM)	Measured [a] (μM)	Recovery [b] (%) (n = 3)	CV [c] (%)
Na_2S	50	53.16	102.43	3.56
	100	98.23	99.75	3.76
	200	196.24	100.59	6.67

[a] Mean value of five independent measurements. [b] Measured value/expected value × 100. [c] Coefficient of variation (CV) = (SD/mean) × 100.

4. Conclusions

We demonstrated that PDA@Co_3O_4 NPs are efficient catalase-like nanozymes, with competitive catalytic activity and stability compared with natural catalase and recently reported catalase-like nanozymes. We also proved that S^{2-} induced highly selective inhibition of the catalase-like activity of the PDA@Co_3O_4 NPs, presumably due to the increased mass transfer limitation through aggregation. Based on the phenomena, S^{2-} was determined with high selectivity and sensitivity, and was quantified in real tap water with sufficient detection precision. This study provides an efficient approach for developing highly efficient nanozymes using simple surface engineering and nanozyme-mediated biosensors. These nanozymes show significant potential for use in diverse biotechnological applications.

Supplementary Materials: The following can be downloaded at: https://www.mdpi.com/article/10.3390/bios12111047/s1, Figure S1: SEM images of (**a**) bare Co3O4 NPs and (**b**) PDA@Co3O4 NPs. Scale bar: 100 nm; Figure S2: TEM images of (**a**) 0.5-PDA@Co3O4 NPs, (**b**) 1-PDA@Co3O4 NPs, and

(**c**) 2-PDA@Co3O4 NPs. Scale bar: 50 nm; Figure S3: XPS spectra of PDA@Co3O4 NPs; Figure S4: Evaluations for the other oxidoreductase-like activities of PDA@Co3O4 NPs and bare Co3O4 NPs. (**a**) POD-, (**b**) OXD- and (**c**) SOD-like activities; Figure S5: Effects of (**a**) concentrations of PDA@Co3O4 NPs, (**b**) pH, and (**c**) temperature on the catalase-like activity of PDA@Co3O4 NPs. Effects of pH and temperature on the activity of natural catalase were compared; Figure S6: (**a**) Michaelis–Menten curve for the catalase-like activity of PDA@Co3O4 NPs at diverse concentrations of H2O2 and (**b**) their corresponding Lineweaver–Burk plots (n = 3); Figure S7: Fluorescence spectra of PDA@Co3O4 NPs-based biosensor toward diverse concentrations of S2−; Figure S8: Particle size distributions of PDA@Co3O4 NPs in the absence and presence of S2− (1 mM); Table S1: Elemental composition ratio of PDA@Co3O4 NPs; Table S2: Comparison of the kinetic parameters of catalase-like PDA@Co3O4 NPs with those of natural catalase and previously reported Co3O4-based nanozymes.

Author Contributions: Conceptualization, investigation, writing—original draft preparation, T.H.V.; validation, writing—review and editing, P.T.N.; and conceptualization, supervision, writing—review and editing, M.I.K. All authors have read and agreed to the published version of the manuscript.

Funding: This work was supported by a National Research Foundation of Korea (NRF) grant funded by the Korean government (Ministry of Science and ICT (NRF-2019R1A2C1087459)). This research was also supported by the Korea Basic Science Institute (KBSI) research (grant number: C280300) and Gachon University research fund of 2021 (grant number: GCU-202110350001).

Institutional Review Board Statement: Not applicable.

Informed Consent Statement: Not applicable.

Data Availability Statement: Not applicable.

Conflicts of Interest: The authors declare no conflict of interest.

References

1. Lefer, D.J. A new gaseous signaling molecule emerges: Cardioprotective role of hydrogen sulfide. *Proc. Natl. Acad. Sci. USA* **2007**, *104*, 17907–17908. [CrossRef] [PubMed]
2. Wei, H.L.; Zhang, C.Y.; Jin, H.F.; Tang, C.S.; Du, J.B. Hydrogen sulfide regulates lung tissue-oxidized glutathione and total antioxidant capacity in hypoxic pulmonary hypertensive rats. *Acta Pharmacol. Sin.* **2008**, *29*, 670–676. [CrossRef] [PubMed]
3. Calvert, J.W.; Jha, S.; Gundewar, S.; Elrod, J.W.; Ramachandran, A.; Pattillo, C.B.; Kevil, C.G.; Lefer, D.J. Hydrogen sulfide mediates cardioprotection through Nrf2 signaling. *Circ. Res.* **2009**, *105*, 365–374. [CrossRef] [PubMed]
4. Kamoun, P.; Belardinelli, M.C.; Chabli, A.; Lallouchi, K.; Chadefaux-Vekemans, B. Endogenous hydrogen sulfide overproduction in Down syndrome. *Am. J. Med. Genet.* **2003**, *116*, 310–311. [CrossRef] [PubMed]
5. McGeer, E.G.; McGeer, P.L. Neuroinflammation in Alzheimer's disease and mild cognitive impairment: A field in its infancy. *J. Alzheimer's Dis.* **2010**, *19*, 355–361. [CrossRef] [PubMed]
6. Suzuki, K.; Olah, G.; Modis, K.; Coletta, C.; Kulp, G.; Gerö, D.; Szoleczky, P.; Chang, T.; Zhou, Z.; Wu, L.; et al. Hydrogen sulfide replacement therapy protects the vascular endothelium in hyperglycemia by preserving mitochondrial function. *Proc. Natl. Acad. Sci. USA* **2011**, *108*, 13829–13834. [CrossRef] [PubMed]
7. Łowicka, E.; Bełtowski, J. Hydrogen sulfide (H_2S)-the third gas of interest for pharmacologists. *Pharmacol. Rep.* **2007**, *59*, 4–24.
8. Radford-Knoery, J.; Cutter, G.A. Determination of carbonyl sulfide and hydrogen sulfide species in natural waters using specialized collection procedures and gas chromatography with flame photometric detection. *Anal. Chem.* **1993**, *65*, 976–982. [CrossRef]
9. Thompson, R.; Perry, J.D.; Stanforth, S.P.; Dean, J.R. Rapid detection of hydrogen sulfide produced by pathogenic bacteria in focused growth media using SHS-MCC-GC-IMS. *Microchem. J.* **2018**, *140*, 232–240. [CrossRef]
10. Balasubramanian, S.; Pugalenthi, V. A comparative study of the determination of sulphide in tannery waste water by ion selective electrode (ISE) and iodimetry. *Water Res.* **2000**, *34*, 4201–4206. [CrossRef]
11. Allen, H.E.; Fu, G.; Deng, B. Analysis of acid-volatile sulfide (AVS) and simultaneously extracted metals (SEM) for the estimation of potential toxicity in aquatic sediments. *Environ. Toxicol. Chem.* **1993**, *12*, 1441–1453. [CrossRef]
12. Jarosz, A.P.; Yep, T.; Mutus, B. Microplate-based colorimetric detection of free hydrogen sulfide. *Anal. Chem.* **2013**, *85*, 3638–3643. [CrossRef] [PubMed]
13. Hatamie, A.; Zargar, B.; Jalali, A. Copper nanoparticles: A new colorimetric probe for quick, naked-eye detection of sulfide ions in water samples. *Talanta* **2014**, *121*, 234–238. [CrossRef] [PubMed]
14. Casella, I.G.; Guascito, M.R.; Desimoni, E. Sulfide measurements by flow injection analysis and ion chromatography with electrochemical detection. *Anal. Chim. Acta* **2000**, *409*, 27–34. [CrossRef]

15. Wang, D.; Wang, Z.; Wang, X.; Zhuang, X.; Tian, C.; Luan, F.; Fu, X. Functionalized copper nanoclusters-based fluorescent probe with aggregation-induced emission property for selective detection of sulfide ions in food additives. *J. Agric. Food Chem.* **2020**, *68*, 11301–11308. [CrossRef]
16. Lawrence, N.S.; Davis, J.; Compton, R.G. Analytical strategies for the detection of sulfide: A review. *Talanta* **2000**, *52*, 771–784. [CrossRef]
17. Gebicka, L.; Krych-Madej, J. The role of catalases in the prevention/promotion of oxidative stress. *J. Inorg. Biochem.* **2019**, *197*, 110699. [CrossRef]
18. Pirmohamed, T.; Dowding, J.M.; Singh, S.; Wasserman, B.; Heckert, E.; Karakoti, A.S.; King, J.E.S.; Seal, S.; Self, W.T. Nanoceria exhibit redox state-dependent catalase mimetic activity. *Chem. Commun.* **2010**, *46*, 2736–2738. [CrossRef]
19. Chen, Z.; Yin, J.-J.; Zhou, Y.-T.; Zhang, Y.; Song, L.; Song, M.; Hu, S.; Gu, N. Dual enzyme-like activities of iron oxide nanoparticles and their implication for diminishing cytotoxicity. *ACS Nano* **2012**, *6*, 4001–4012. [CrossRef]
20. Mu, J.; Zhang, L.; Zhao, M.; Wang, Y. Catalase mimic property of Co_3O_4 nanomaterials with different morphology and its application as a calcium sensor. *ACS Appl. Mater. Interfaces* **2014**, *6*, 7090–7098. [CrossRef]
21. Mu, J.; Zhang, L.; Zhao, M.; Wang, Y. Co_3O_4 nanoparticles as an efficient catalase mimic: Properties, mechanism and its electrocatalytic sensing application for hydrogen peroxide. *J. Mol. Catal. A—Chem.* **2013**, *378*, 30–37. [CrossRef]
22. Zandieh, M.; Liu, J.J.L. Surface Science of Nanozymes and Defining a Nanozyme Unit. *Langmuir* **2022**, *38*, 3617–3622. [CrossRef] [PubMed]
23. Lee, H.; Dellatore, S.M.; Miller, W.M.; Messersmith, P.B. Mussel-inspired surface chemistry for multifunctional coatings. *Science* **2007**, *318*, 426–430. [CrossRef] [PubMed]
24. Liu, X.; Cao, J.; Li, H.; Li, J.; Jin, Q.; Ren, K.; Li, J. Mussel-inspired polydopamine: A biocompatible and ultrastable coating for nanoparticles in vivo. *ACS Nano* **2013**, *7*, 9384–9395. [CrossRef]
25. Jiao, L.; Xu, W.; Yan, H.; Wu, Y.; Gu, W.; Li, H.; Du, D.; Lin, Y.; Zhu, C. A dopamine-induced Au hydrogel nanozyme for enhanced biomimetic catalysis. *Chem. Commun.* **2019**, *55*, 9865–9868. [CrossRef]
26. Niyonshuti, I.I.; Krishnamurthi, V.R.; Okyere, D.; Song, L.; Benamara, M.; Tong, X.; Wang, Y.; Chen, J. Polydopamine surface coating synergizes the antimicrobial activity of silver nanoparticles. *ACS Appl. Mater. Interfaces* **2020**, *12*, 40067–40077. [CrossRef]
27. Zhang, N.; Peng, S.; Liu, Z.; Li, Y.; Huang, J.; Li, J.; Wan, H.; Zhou, S.; Gao, Z.; Chen, T. Ag NPs decorated on the magnetic Fe_3O_4@PDA as efficient catalyst for organic pollutants removal and as effective antimicrobial agent for microbial inhibition. *J. Alloy. Compd.* **2022**, *928*, 167257. [CrossRef]
28. Yang, H.; Zhao, X.; Zhang, Z.; Ma, P.; Wang, X.; Song, D.; Sun, Y. Biotin-streptavidin sandwich integrated PDA-ZnO@Au nanocomposite based SPR sensor for hIgG detection. *Talanta* **2022**, *246*, 123496. [CrossRef]
29. Siciliano, G.; Monteduro, A.G.; Turco, A.; Primiceri, E.; Rizzato, S.; Depalo, N.; Curri, M.L.; Maruccio, G. Polydopamine-coated magnetic iron oxide nanoparticles: From design to applications. *Nanomaterials* **2022**, *12*, 1145. [CrossRef]
30. Tavakoli, S.; Kharaziha, M.; Nemati, S. Polydopamine coated ZnO rod-shaped nanoparticles with noticeable biocompatibility, hemostatic and antibacterial activity. *Nano-Struct. Nano-Objects* **2021**, *25*, 100639. [CrossRef]
31. Dou, S.; Tao, L.; Huo, J.; Wang, S.; Dai, L. Etched and doped Co_9S_8/graphene hybrid for oxygen electrocatalysis. *Energy Environ. Sci.* **2016**, *9*, 1320–1326. [CrossRef]
32. Zhao, H.; Zeng, Z.; Liu, L.; Chen, J.; Zhou, H.; Huang, L.; Huang, J.; Xu, H.; Xu, Y.; Chen, Z.; et al. Polydopamine nanoparticles for the treatment of acute inflammation-induced injury. *Nanoscale* **2018**, *10*, 6981–6991. [CrossRef]
33. Zhang, X.Q.; Gong, S.W.; Zhang, Y.; Yang, T.; Wang, C.Y.; Gu, N. Prussian blue modified iron oxide magnetic nanoparticles and their high peroxidase-like activity. *J. Mater. Chem.* **2010**, *20*, 5110–5116. [CrossRef]
34. Purbia, R.; Paria, S. Green synthesis of single-crystalline akaganeite nanorods for peroxidase mimic colorimetric sensing of ultralow-level vitamin B1 and sulfide ions. *ACS Appl. Nano Mater.* **2018**, *1*, 1236–1246. [CrossRef]
35. Rajamanikandan, R.; Ilanchelian, M. Simple smartphone merged rapid colorimetric platform for the environmental monitoring of toxic sulfide ions by cysteine functionalized silver nanoparticles. *Microchem. J.* **2022**, *174*, 107071. [CrossRef]
36. Gao, Z.; Tang, D.; Tang, D.; Niessner, R.; Knopp, D. Target-induced nanocatalyst deactivation facilitated by core@shell nanostructures for signal-amplified headspace-colorimetric assay of dissolved hydrogen sulfide. *Anal. Chem.* **2015**, *87*, 10153–10160. [CrossRef]